The Planetary Science Journal, 5:115 (13pp), 2024 May https://doi.org/10.3847/PSJ/ad3df4

Dry Downhill Particle Motion on Mars

Tetyana Bila, Gerhard Wurm, Kai Stuers, Kolja Joeris, and Jens Teiser
University of Duisburg-Essen, Faculty of Physics, Lotharstr. 1, 47057 Duisburg, Germany
Received 2023 November 1; revised 2024 March 22; accepted 2024 April 10; published 2024 May 15

Abstract

We recently flew a new setup on parabolic flights for the first time to study particle motion on Martian slopes under Martian gravity. Here, we describe the initial experiments. We used dust/sand beds at varying ambient pressure of a few hundred pascals. The inclination of the particle bed was varied from 0° to 45° and parts of the surface were illuminated under varying conditions. We could observe downhill motion of material related to the insolation at the lowest light flux used of $591 \pm 11\,\mathrm{W\,m^{-2}}$ for JSC Martian simulant. Motion occurred at significantly lower inclinations under illumination than without illumination, i.e., down to about 10° compared to about 20°–30°, respectively. We attribute this reduction in slope to thermal creep gas flow in the subsoil. This induces a Knudsen compressor, which supports grains against gravity and leads to smaller angles of repose. This is applicable to recurring slope lineae and slopes on Mars in general.

Unified Astronomy Thesaurus concepts: Planetary science (1255); Planetary surfaces (2113); Mars (1007)

1. Introduction

Much of the surface of Mars is covered by dust and sand, and ways to mobilize these grains are important for many studies. The scientific problems range from the entrainment of dust into the atmosphere by wind and saltation, dust devils, or electrostatics (Greeley et al. 1980; Cantor et al. 1999; Montabone et al. 2005; Kok & Renno 2008; Kok et al. 2012; Reiss & Lorenz 2016; Becker et al. 2022; Lorenz 2023; Toledo et al. 2023) to the formation of geomorphologic features like dunes (Chojnacki et al. 2011; Bridges et al. 2012a, 2012b; Kok et al. 2012). Quite generally, mobilization is important for all kinds of slopes on Mars because their angle is set by downhill motion. We only consider dry flows here, though wet flows might play their part in particle motion (Philippe et al. 2023).

With more or less cohesive granular material, there is a maximum inclination, the angle of repose, before material starts to avalanche downward on a slope in a static setting or stops flowing downward in the dynamic case. Visible signs of granular flows that receive quite some attention are recurring slope lineae (RSL). These streaks show up and vanish again in some cycle over time (McEwen et al. 2011; Chojnacki et al. 2016). McEwen et al. (2021) argue that their occurrence might be related to global dust storms, which might then be considered to refill the slopes with material just to move downward somewhat later. Dundas (2020) concludes that they can well be explained as aeolian grainflow. There are also less specific models but they also somewhat favor external replenishment (Stillman et al. 2021).

There have been some discussions as to whether slopes showing RSL activity are lower than slopes found on Earth (Schmidt et al. 2017; Stillman et al. 2020; Tebolt et al. 2020). Considering some to be typical statistical outliers, most slopes might be consistent with slopes observed on Earth (Dundas 2020; Stillman et al. 2020). Some complexities or details might be added, e.g., by the mechanism outlined in this paper. Gravity-independent slopes, i.e., ones that are the same on Mars and Earth, have also been reported for the slip faces of active dunes (Atwood-Stone & McEwen 2013; Ewing et al. 2017). In particular, the rover measurements also give here a grain size of about 100 μm (Atwood-Stone & McEwen 2013). There are other types of features, e.g., slope streaks, where the question also arises as to what triggers them and sets the inclination of the slope (Aharonson et al. 2003; Schorghofer & King 2011; Heyer et al. 2020; Dundas 2021; Lange et al. 2023). Slopes seem notably smaller here.

The conditions under which particle motion on slopes is triggered on Mars are the focus of this work. These might be related to slope angles in general or in detail. They might also just add a component of (small-scale) surface flow that might go unnoticed in slope angles but might be important for dust entrainment into the atmosphere. We present experiments under conditions simulating Martian gravity, Martian pressure, and Martian insolation. We determine thresholds for particle motion as we increase the slope of a particle bed. We specifically study thermal creep gas flow induced by the illumination, which might strongly reduce the necessary angles, as it supports the grains by a sub-surface overpressure. This mechanism is outlined in the following section.

2. Thermal Creep and Granular Knudsen Compressor

On Earth, gas dynamics within the atmosphere or within soils is determined by the usual hydrodynamics. While this might also become complex, there are some rather simple rules. If, for example, the atmospheric pressure in two adjacent locations is different, there will be a gas flow from high to low pressure until the pressure is balanced. If two parts are in equilibrium and one part is heated, gas flows from this heated region because pressure increases and again drives the gas flow. This is also the case for most of Mars. However, these simple rules do not apply to Martian soil due to something called "thermal creep." Thermal creep in natural soils is complex. Therefore, in the following subsections, we explain and visualize how thermal creep, Knudsen compressors, and the related lifting force on grains work in principle. We go from idealized laboratory settings of simple tubes and gas reservoirs to granular settings to Mars.

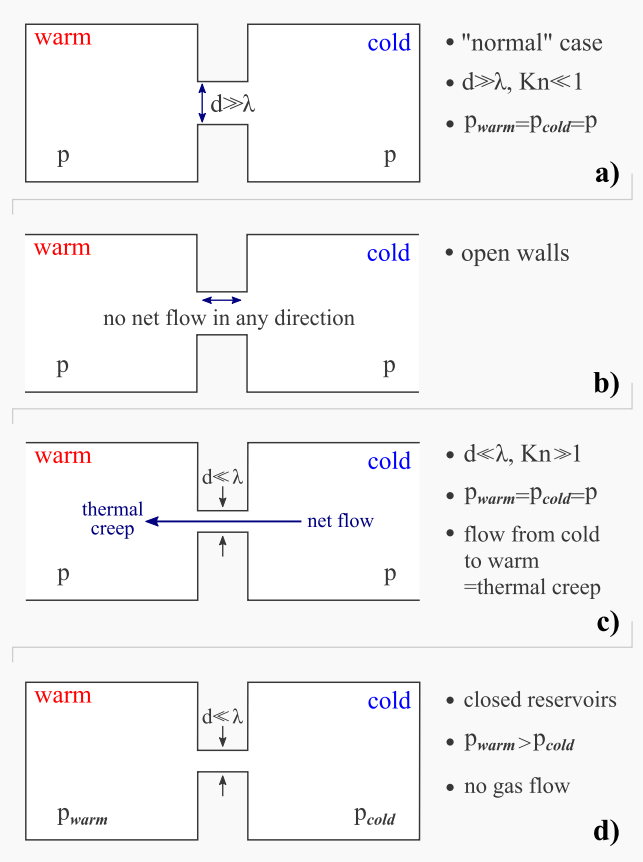

Figure 1. Sketch of how thermal creep and Knudsen compressors work in an idealized equilibrium setting. (a), (b) A large connection between two reservoirs leads to the same pressure within. (c) Thermal creep for a small connection drives flow from the cold to the warm side. (d) For a closed system, in equilibrium, the pressure on the warm side increases and the flow subsides.

Thermal creep is the process underlying the motivation of this work. We note that we talk about a gas flow within the pores of the Martian soil here (Koester et al. 2017). This is not to be confused with the very slow particle motion of a granular medium itself due to temperature variations and associated small shifts of the grains, which also goes by the name thermal creep (Divoux et al. 2008; Deshpande et al. 2021).

2.1. Idealized Setting

Thermal creep gas flow is tied to the relation between the mean free path length (λ) of gas on one side and the size (d) of a structure embedding the gas on the other side. This is the Knudsen number $Kn = \lambda/d$. Thermal creep becomes effective at about $Kn \sim 1$ and higher. Thermal creep also needs a temperature difference between adjacent locations. Figure 1 visualizes the situation. In panel (a) a "normal" hydrodynamic setting is shown for equilibrium. Two reservoirs at different temperatures are connected by a tube of large diameter. Any difference in pressure is balanced by a flow through the tube until the pressure is equilibrated and the gas flow stops. This situation remains unchanged if the reservoirs are opened to a large "infinite" gas reservoir (panel (b)). There is only one pressure and no gas flow. In panel (c) the connecting tube is reduced in size until the Knudsen number becomes large. Alternatively, the pressure could be reduced. In any case, gas now flows from the cold to the warm side. In the infinitely large reservoir setting, this does not change the pressure. It also

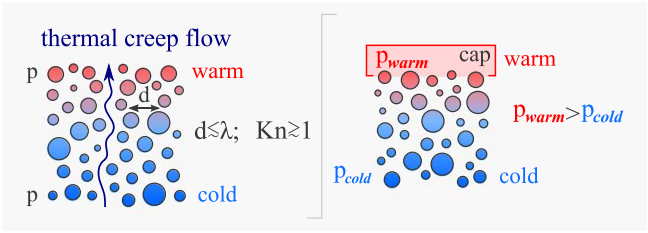

Figure 2. Thermal creep in a granular setting. If the top is capped, i.e., has a finite reservoir, pressure increases.

means that thermal creep needs no pressure difference to drive it.

Figure 1(c) does not explain how thermal creep works, just what it does. A heuristic explanation would be as follows. In both reservoirs, left and right, normal rules for an ideal gas apply. In the connecting tube, though, there are no molecular collisions due to the large Knudsen number. Therefore, the net flow is the difference between the flow from cold to warm and the opposing flow. This can be estimated from the number of molecules hitting the entrance of the tube per unit time, which results in a net flow from the cold to the warm side.

In Figure 1(d) the reservoirs are closed again. Naturally, the thermal creep flow now leads to a pressure increase on the warm side. This pressure difference drives a backflow to the cold side. The pressure difference increases until this backflow equals the thermal creep flow.

In the early 20th century, Knudsen (1909) set up similar arrangements. Therefore, systems at low pressure, which move gas by thermal creep or produce pressure variations, are often referred to as Knudsen compressors (Vargo et al. 1999; Muntz et al. 2002).

2.2. Granular Soil Settings

Small connecting tubes are an ideal. However, thermal creep works for any shape of structure as long as the size of the cavities or pores is of the order of or smaller than the mean free path of the gas molecules. A granular medium consisting of dust or sand can be considered as a generalized setting where grains provide the walls for the pore space, which is equivalent to the tubes in the simple setting. This situation is visualized in Figure 2. The two situations shown correspond to the simple settings where either there is a flow between two infinite reservoirs at the same pressure or at least one side of the granular medium is capped, i.e., holds a reservoir of finite volume. In the latter case, the pressure increases on the warm side again.

2.3. Natural Setting on Mars with Constant Illumination

Insolation of a natural surface is one way to generate a temperature gradient within a granular medium as the top is heated and the deeper layers stay cooler. However, the temperature distribution within the soil is not linear. The top layer is subject to a solid-state greenhouse effect (Kaufmann et al. 2006; Wurm & Krauss 2006; Kocifaj et al. 2011; Attree et al. 2021). That is, the visible solar radiation is partially absorbed in layers below the surface but only the very top of the soil can cool by thermal radiation. As a result, the temperature has a rather flat plateau at the top (all warm) as indicated in Figure 3. Thermal creep does not occur in this constant-temperature section. This top layer is like the cap in

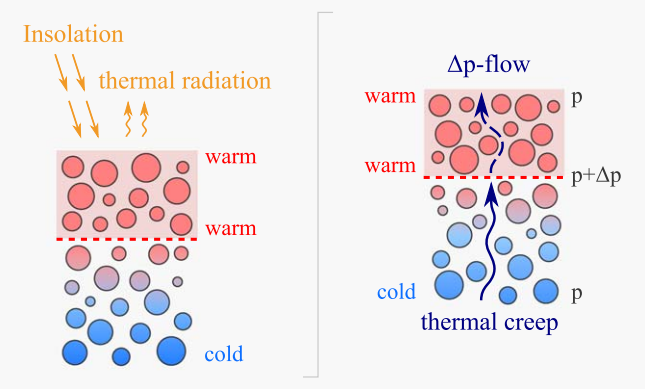

Figure 3. Thermal creep on Mars under insolation. Due to the solid-state greenhouse effect, the top layers show little temperature variation and do not allow thermal creep. Thermal creep gas flowing from below has to generate a pressure increase that drives the flow through the surface layers.

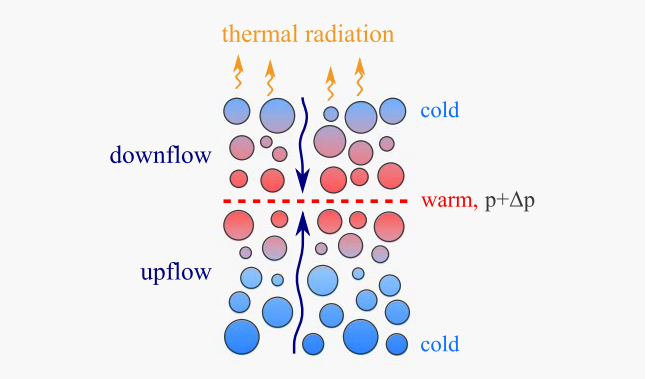

Figure 4. Thermal creep on Mars if the insolation is turned off. As the surface cools, a second Knudsen compressor also pumps gas downward to the temperature maximum. This increases the sub-surface pressure further.

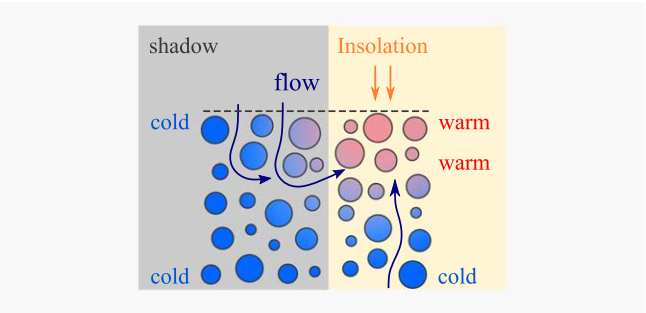

Figure 5. Thermal creep on Mars if a shadowed region is close by. Now gas can also be provided from regions to the side. In a setting without a large underground gas reservoir, this can increase the thermal creep gas flow.

Figure 2 but, as a porous medium, this cap is leaky. So the final state is reached once the pressure under the top millimeter or so is increased enough to transport the same amount of gas by the overpressure as the amount that arrives by thermal creep flow from below.

This pressure gradient now also supports the grains within the soil and provides a lifting force on them. This topmost pressure-supported layer of a few millimeters thickness has recently been visualized by Bila et al. (2023) using diffusive wave spectroscopy. The activated top layer under tension was also shown in experiments in de Beule et al. (2015). The works on particle lift showed that the pressure adjusts on timescales of seconds or less (Kelling et al. 2011; de Beule et al. 2014). It is this grain support by upward-directed pressure gradients that should decrease the angle of repose because a net downhill force is more readily reached, at least for this topmost layer (see sections below).

2.4. Time-varying Illumination

The temperature gradient close to the surface of the soil is dependent on the general timing of the illumination. Clouds might be a candidate here to modulate the insolation; maybe on Mars it might rather be the shadow of a dust devil, the dust devil itself, or albedo changes induced by the dust devil (Reiss et al. 2010; Heyer et al. 2020; Vicente-Retortillo et al. 2023). One might argue that the dust devil would do the job of releasing grains already. However, it might only trigger an avalanche, which might then be amplified by self-shadowing.

Anyway, if insolation is turned off or significantly reduced, cooling by thermal radiation will prevail. This can reverse the temperature gradient at the top as indicated in Figure 4. Gas flow from the Knudsen compressor below is not only hindered now but the top acts like a second Knudsen pump pumping downward against the first Knudsen pump. The pressure maximum below the surface has to increase (Kelling et al. 2011; Kocifaj et al. 2011; Kuepper & Wurm 2016).

To get an impression of the small size scales needed, it might be illustrative to see that even small submillimeter aggregates of only tens of grains can hold a Knudsen compressor (Musiolik et al. 2017). Once ejected from a hot surface, they cool from the outside in. At low ambient pressure, this generates an inner overpressure by thermal creep that is capable of exploding the aggregate on timescales of less than a second (Musiolik et al. 2017).

2.5. Spatially Inhomogeneous Illumination

Somewhat similarly to the time-varying case, spatial variations in illumination, e.g., transitions due to long-lived shadows of a cliff or albedo variations in general, are also important for thermal creep and might increase the sub-surface pressure. Amplification might occur in these cases because there would not be a homogeneous upward flow. Such an upward flow ultimately needs some gas reservoir somewhere deeper in the ground. In a heterogeneous case the gas could flow from nearby dark places overall, resulting in less resistance to the flow. It has, for example, been shown by de Beule et al. (2014) that gas flows down into the ground in dark nonilluminated places and flows upward within an illuminated spot. This is visualized in Figure 5.

This shadowing has been proposed by Schmidt et al. (2017) to explain low angles of repose for RSLs on Mars. And in fact, this proposal by Schmidt et al. (2017) was the original motivation for the work reported here. However, compared to some previous work on time-varying insolation, Knudsen compressors related to spatial variations are currently almost completely uncharted terrain apart from the proposal by Schmidt et al. (2017). Alternatively, cracks, which might not be large but rather on the millimeter scale, being just too wide for thermal creep transport, might ease gas flow into a Knudsen compressor within illuminated soil nearby.

In any case, illumination of various kinds would add forces to grains within the soil and this might trigger particle motion. This might or might not change the static angle of repose. It might be a function of gravity, depend on the specific soil parameters, and vary with illumination details.

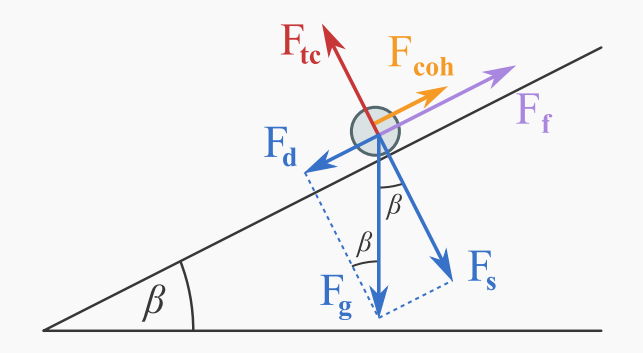

Figure 6. Basic force balance depending on the inclination.

2.6. Knudsen Numbers on Mars

We noted that thermal creep is strongly tied to large Knudsen numbers. Effects for granular beds are most pronounced for $Kn \sim 1$ but they are also noticeable for $Kn \leqslant 0.1$ (Koester et al. 2017). At very large Knudsen numbers, i.e., very small grains, the flow would just no longer be significant (Koester et al. 2017).

With a surface pressure of a few hundred pascals, the mean free path length of gas molecules on Mars is of the order of 10 μm and therefore within the range of the dust and sand and pore size within the Martian soil. The process therefore is unique to the Martian surface, at least for planets in our solar system. This makes it interesting but also means that experience from Earth is lacking as a guide for a potential application to Mars.

The fact that the grain and pore sizes are of the same order of magnitude as the mean free path of the gas molecules also means that the specific local soil conditions and ambient pressure either do allow or do not allow the thermal creep to work. Dunes with grains of 100 μm or more might not show any effects of thermal creep, while dust-laden surfaces might readily react. To evaluate all conditions for Mars is beyond the scope of this paper though.

3. Angle of Repose

Our definition of the inclination, β, of the particle bed as simulated soil can be taken from Figure 6, which is also a rough sketch of relevant forces.

In a simple setting, the static angle of repose β_r is just the inclination where the downhill force F_d due to gravity balances the restricting friction force F_f. The downhill component of gravity is calculated straightforwardly as

$$F_d = F_g \sin(\beta) = m g_p \sin(\beta). \tag{1}$$

Here, m is the grain mass and g_p is the gravitational constant of the given planet. The friction force depends on the force acting normal to the surface. In the case of only gravity, this is F_s and the friction force is

$$F_f = \alpha F_s = \alpha F_g \cos(\beta) = \alpha m g_p \cos(\beta), \tag{2}$$

where α is the friction coefficient. This leads to the usual condition for the angle of repose for a cohesionless granular medium:

$$\tan(\beta_r) = \alpha. \tag{3}$$

This equation does not explicitly depend on gravity as the dependence of both forces on g_p cancels out. This is important to note because in the case of purely large noncohesive grains, as outlined above, pore and grain size might be too large for thermal creep to act.

For smaller grains, and especially soils with larger amounts of dust included, there are additional forces. Cohesion becomes important, eventually. At the level of individual grains, this can, for example, be quantified by the pull-off force between two grains, which for spherical grains is $F_p = 3\pi\gamma r/2$ (Johnson et al. 1971). Depending on the contacts, the direction might vary and additional components to rolling and sliding might occur. To simplify things, we just include cohesion as a force opposing the downhill motion here as $F_{\rm coh}$. The point we would like to make is that cohesion does not depend on gravity but on surface energy γ (material) and particle radius r. This removes the degeneracy on gravity g_p, introducing a gravity dependence. Numerical simulations also suggest such gravity dependences for cohesive matter (Elekes & Parteli 2021). Also, microgravity experiments by Kleinhans et al. (2011) show strong gravity dependence, though their grains are large and supposedly noncohesive. How this fits with the fact that the slip faces of dunes on Mars seem to show similar values to those on Earth, as found by, e.g., Atwood-Stone & McEwen (2013), is an open question.

However, there are further differences between Earth and Mars apart from gravity. The atmospheric pressure is the important one for this work. This introduces another upward-directed force due to thermal creep $F_{\rm tc}$ as outlined above.

Adding these other forces specifically, and considering α not to depend on cohesion, we get as balance:

$$F_d = \alpha(F_s - F_{\rm tc}) + F_{\rm coh}. \tag{4}$$

To distinguish the angle of repose for the case of cohesion, we add an index "c" and call the angle $\beta_{\rm rc}$. Inserting the specific forces then yields

$$m g_p \sin(\beta_{\rm rc}) = \alpha m g_p \cos(\beta_{\rm rc}) - \alpha F_{\rm tc} + F_{\rm coh}, \tag{5}$$

or

$$\sin(\beta_{\rm rc}) - \alpha \cos(\beta_{\rm rc}) = \frac{F_{\rm coh} - \alpha F_{\rm tc}}{m g_p}. \tag{6}$$

The left-hand side increases monotonically with $\beta_{\rm rc}$. That means that the angle of repose should increase with decreasing gravity, which fits with simulations (Elekes & Parteli 2021); note that experiments on this show more complex behavior (Kleinhans et al. 2011). The static angle of repose should also decrease with an active Knudsen compressor, which is our focus here.

Insolation-induced granular Knudsen compressors and the response of the soil are quite complex to calculate. Here, they would require the calculation of temperature profiles in a setting of heat transfer by conduction and radiation in a granular medium, which is nontrivial. They would require the calculation of gas flow in a low-pressure setting with a mixture of free molecular flow, thermal creep, and continuum hydrodynamics, which is also nontrivial and a problem of its own. They would also require the calculation of all forces on the grains to deduce a possible angle of repose or conditions for particle motion. Koester et al. (2017) give a model for a granular Knudsen compressor, which might be extended in the future to describe Martian soil. For now, a quantitative model will be beyond the scope of this paper. Our intention is to pin

down any effect on the angle of repose at all in experiments beyond mere plausibility.

4. Experiments

The rationale behind the experiment is the attempt to mimic slopes on Mars as well as possible, inclining slopes ever further until particles move downhill. To achieve this, the experiment in principle works as follows. We take a Martian soil simulant (sand/dust) and place it within a container. This container is horizontally vibrated at a frequency of 10 Hz and an amplitude of 2 mm to generate a flat surface. The duration of the vibrations is not fixed but is on a timescale of seconds; the vibration continues until visual inspection suggests that the particle bed is flat.

The container is located within a vacuum chamber. This chamber is evacuated to pressures of a few millibars to be within the range of pressures on the Martian surface. To simulate Martian gravity, this vacuum chamber is attached to a centrifuge. Rotation produces a centrifugal acceleration, which we set to the Martian value of $0.38g$, with g being Earth's gravity. The axis of the centrifuge is vertical. Therefore, the centrifugal force is orthogonal to Earth's gravity. The centrifuge is operated within an aircraft that carries out parabolic maneuvers. That means, in straight flight, a net acceleration of $1.05g$ acts on the sample. In order to inject into a parabola, the plane then accelerates upwards at about $1.8g$ vertically. The net acceleration on the sample is about $1.83g$ in this phase for 20 s. The plane then enters a phase of microgravity with residual accelerations of the plane of the order of $0.01g$. In this phase, the sample is subject to the remaining centrifugal acceleration only or the Martian value of $0.38g$. This phase of Martian gravity lasts for about 20 s.

With the onset of Martian gravity, the dust bed's inclination is raised at a constant rate of a few degrees per second, i.e., at about $2^\circ\ s^{-1}$. Final inclinations of about 40° are reached within the 20 s of Martian gravity. To induce thermal creep, a part of the simulated soil is illuminated with the light of a halogen lamp focused into a spot of a few centimeters in diameter. The soil is observed from above with a camera in visible light and a thermal infrared camera. After Martian gravity, the plane enters another 20 s flight with $1.8g$, after which it resumes straight flight of $1g$. Movies of the visual camera are analyzed postflight to detect the downhill motion of particles. Basic results of one of the parabolas are the motion events of particles depending on the inclination angle of the particle bed. These events are further related to the various parameters.

4.1. Parameter Variations

Parabolas are repeated 31 times on a single flight with varying $1g$ time in between. Typically, the flight times in straight flight ($1g$) between two parabolas are of the order of 2 minutes. There are $1g$ phases of 5 minutes every five parabolas, and a pause of 8 minutes in the middle of the flight. These times in between parabolas are used to adjust parameters. There are two vacuum chambers on opposite sides of the centrifuge, and the experiment flew on three days. In total this gives potentially 2×93 parabolas to collect data on particle motion for various parameters. However, due to the large number of possible parameters and their combinations and the idea of scanning this parameter space, this can only be considered a first approach. Parameter combinations were varied in the ranges given in Table 1.

Table 1
Parameters and Ranges of Values Used

Parameter	Range	Remark
Gravity	$3.7\ m\ s^{-2}$	Martian gravity
Ambient pressure	204, 573, 603 Pa	averages
Inclination	0–45°	⋯
Inclination rate	$1–3^\circ\ s^{-1}$	⋯
Initial inclination	0, 20°–30°	⋯
Light flux	$591, 1028, 1235\ W\ m^{-2}$	⋯
Light modulation	various	on/off, timing
Simulant	JSC, MGS, basalt	⋯
Grain size	10–1000 μm	depends on simulant

4.2. Detailed Experimental Setup

A sketch of important parts of the setup is shown in Figure 7. The mounting structure is not shown. In the following subsection we detail some of the aspects mentioned in the general description of the experiment given above.

Martian gravity. This is simulated by means of a centrifuge. According to $a = R\omega^2$, with R the distance from the location of the particle bed to the rotation axis and ω the circular frequency, a centrifugal acceleration a can be set to Martian values g_M. On the ground, with a vertical rotation axis, this is oriented horizontally and adds like a vector to Earth's gravitational acceleration $g_E = g$ pointing downward. Because the sample is placed in a chamber that is attached to a structure that can pivot in the direction of the total force, the acceleration on the pivoting structure always points "downward," setting a reference direction.

Unfortunately, on the ground, values smaller than $1g$ cannot be reached. Therefore, the whole setup is placed in a plane that flies parabolic maneuvers, i.e., is free-falling for about 20 s. This removes g_E, and the sample pivots further and leaves g_M as acceleration, keeping in mind that R changes and ω had to be chosen for the R acting at that point.

Added to this centrifugal acceleration is the so-called g-jitter of the airplane, which is not predictable; it depends on the flight maneuvers, which depend on the weather conditions and pilots, but is usually of the order of $\pm 0.01g$ during a parabola. The g-jitter has a different direction than the centrifugal acceleration. Due to the rotation of the setup, this adds random and harmonic modulations to the basic Martian value at the g-jitter level. Two examples of the experimental acceleration simulating gravity over time are shown in Figure 8 (top blue lines).

It has to be noted that we do not consider Coriolis forces here, which are not important as long as the particles are not moving.

Martian pressure. The chamber that holds the sample is a vacuum chamber. Its pressure can be set to Martian values, i.e., from below 100 Pa to anything larger. To achieve this, we use a pump to decrease the pressure as well as a rated valve to increase the pressure (not visible in Figure 7). We currently use unprocessed air. Densities and free path lengths of molecules at a given pressure depend on the gas composition, i.e., they would change in the case of CO_2 simulating the Martian atmosphere instead of using air. The principal idea of the Knudsen compressor will not change. It should be kept in mind

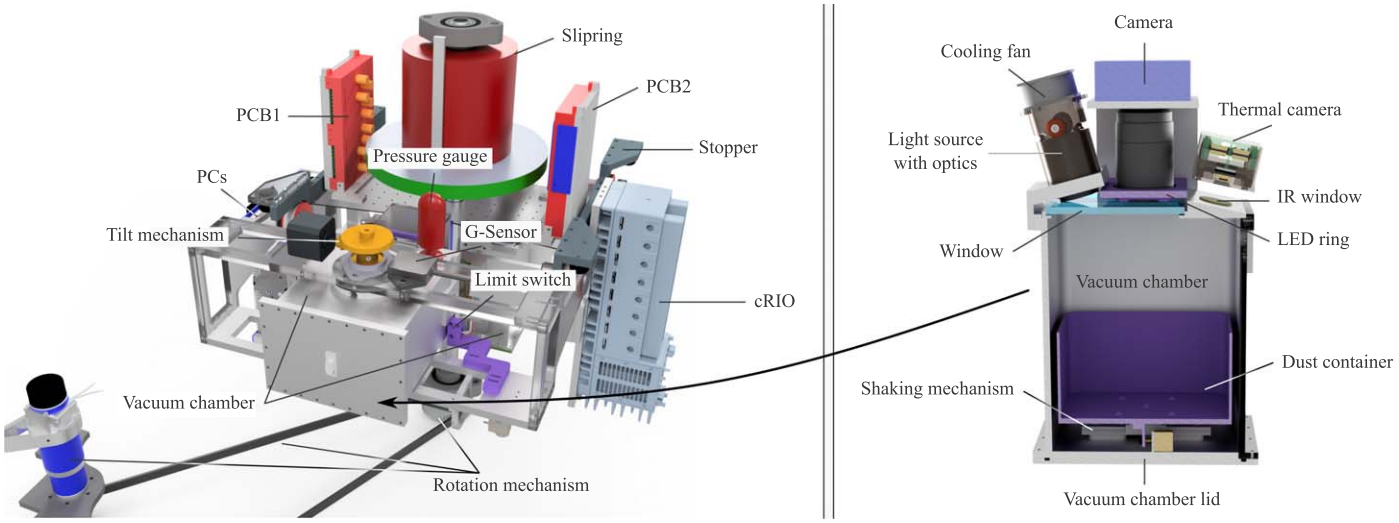

Figure 7. Sketch of the experimental setup. The chamber marked as the vacuum chamber (left) is shown in detail on the right. Specific components on the left: Tilt mechanism—motor and gear to incline vacuum chamber; Limit switch—limits maximum tilt angle; Rotation mechanism—motor and belt to drive vertical axis; Slip ring—on vertical axis to provide electrical feedthroughs to rotating devices; Pressure gauge—measures ambient pressure in vacuum chamber; G-sensor—measures acceleration at soil level; Stopper—restricts the pivoting of the vacuum chamber; cRIO—controlling computer; PCB1 and PCB2—electronic boards; PCs—computer to record camera images; not visible (hidden) but essential is also a vacuum pump. Right: attached to the vacuum chamber are: Light source with optics and cooling—simulates Sun and provides heating of soil; Camera and LED ring—images soil surface and particle motion; Thermal camera with Infrared window—determines surface temperature; Shaking mechanism—laterally shakes dust container to level soil surface; Vacuum chamber lid—dedicated opening to exchange samples between flights. For reference, the inner size of the dust container is 125 mm × 75 mm.

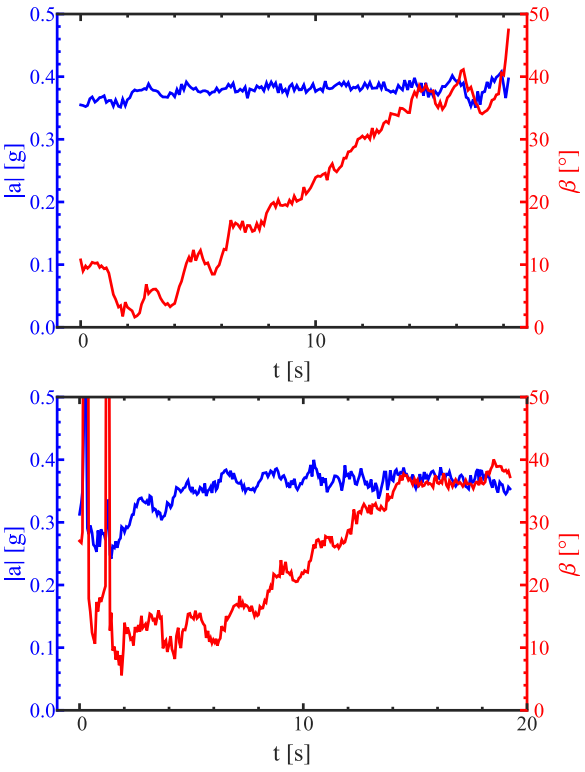

Figure 8. Two examples of the absolute value of the acceleration over time (left axis, top blue curve) and the slope of the particle bed (right axis, bottom red curve) during one parabola. Top: parabola Nr. 17, day 1, overall lower g-jitter values. Bottom: parabola Nr. 28, day 1, higher g-jitter values during the first two seconds of the Martian gravity setup.

though that exact values, i.e., pressures and particle sizes for maximum effects, depend slightly on this. This is not important in this first study but has to be considered once a sufficient database for quantitative statements can be given.

Martian insolation. A halogen lamp is mounted on top of the vacuum chamber. It is focused into a spot of about 20 mm in diameter with a sharp transition at the edge of the spot. This is a small part of the total area of the particle bed of 125 mm × 75 mm. The lamp provides a light flux of up to 1235 W m^{-2}.

Martian slopes. In addition to the basic setting, the chamber can be inclined, varying the slope of the sample within. We varied the slope of the particle bed within each parabola in different intervals and at rates of 2–3° s^{-1}. In general, we quantify the strength of any motion event depending on the inclination of the particle bed at that time. As outlined below, we do not see a single failure of the slope at a single angle of repose but detect motions of particles on the surface in various locations, which can be distinct and not influence each other. So there can be several different events in one parabola and one sample as the angle is constantly increased. An example of the slope over time can also be seen in Figure 8. As the main angle, it shows the angle we set by inclination. Added components originate from the g-jitter.

We note that a flat particle bed with a slope of zero is assumed at the onset of each parabola. This is achieved by horizontally shaking the sample in 1g.

Due to the limited amount of data and the small deviations of the absolute value from Martian gravity, we consider all values to be taken at Martian gravity. However, as just mentioned, we do take the g-jitter into account for determination of the exact slope angle. To do so we define the angle β as follows:

$$\beta = \arccos(a_x \cos\alpha + a_y \sin\alpha), \tag{7}$$

with a_x and a_y being the x- and y-components of the acceleration as measured by the sensors and α the set inclination angle.

4.3. Soils

Thermal creep and downhill flow depend on the specific soil. If grains are too large, pores are too large for thermal creep. If

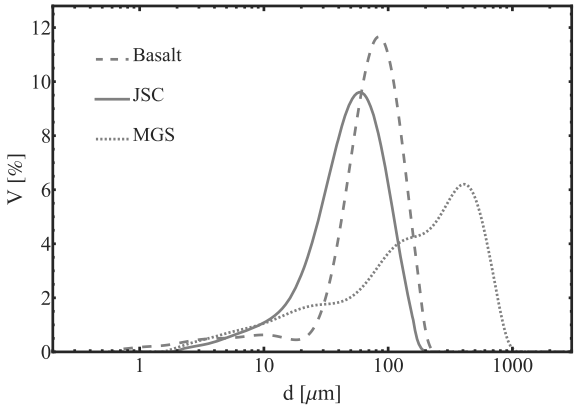

Figure 9. Size distributions of the samples used. Continuous line: JSC, dashed line: basalt, dotted line: MGS.

the grains are too small, cohesion prevents particle flow. As the number of parameters that can be tested in one parabolic flight campaign is limited, we chose three different samples of dust and sand from typical Martian simulants as an initial set to test whether any effects of a given slope on particle motion would be visible. Specifically, we chose:

1. JSC Mars 1a: this is a palagonite sample from Hawaii that was distributed by the Johnson Space Center for some time, especially due to its color. We sieved the sample to sizes smaller than 125 μm. For drying it was heated to 120°C overnight.
2. Basalt: we used a commercial basalt sample here (Kremer Pigmente) and also sieved this to sizes smaller than 125 μm and heated it to 120°C overnight to dry.
3. Mars Global Simulant (MGS-1): As the third sample we used an artificial mineral composition from plagioclase, pyroxene, basaltic glass, olivine, and other components mixed together in different proportions (Cannon et al. 2019). This sample was not sieved and not further processed before use.

The size distributions of the samples are shown in Figure 9 as measured by a particle size analyzer (MasterSizer 3000).

5. First Results

5.1. Downhill Particle Motion

Equation (6) implies a clear definition of the angle of repose and we would have expected to see clear slope failures at angles well below 40° in detail, depending on illumination or not. In contrast to these expectations, we did not detect the whole slope slipping downward even up to the maximum angle of 45° that the experiment provided. However, we detected local downhill motion of particles in various locations and for various strengths of the surface.

Figure 10 is a visualization of an example of motion not initiated by the illumination, i.e., triggered by inclining the slope only. Particle motion can be discerned in the original movies, but as the surface is rather featureless and particle motions sometimes include only small locations or distances, we processed the images to highlight the motion. We calculated the displacements of particles compared to the initial image at the onset of Martian gravity. The calculated displacement images are then summed, normalized to the maximum being 1, and color-coded. This results in an image where bluish areas

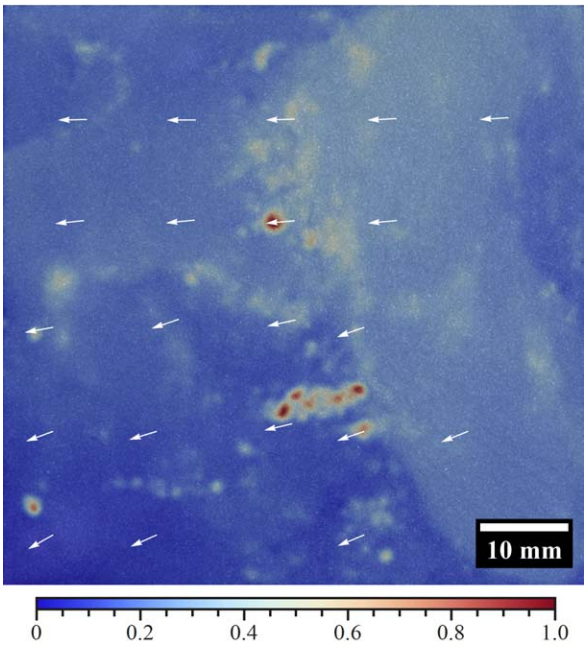

Figure 10. Particle motion in parabola Nr. 17 (first day). Shown by color coding is the sum of a number of events in a part of the nonilluminated basalt particle bed. The image visualizes the change in the sample surface between a later image and the earlier image of the sample during the parabola, i.e., highlighting the motion. For better visibility the image is further contrast-enhanced. Arrows indicate the direction of motion. Visible is a large area slowly moving downwards and a number of more local particle motions.

symbolize areas with no movement (displacement 0), whereas yellow to red colors show displaced areas (red: displacement 1). The example of Figure 10 shows a slight shift of a larger region on the right (pale yellow) and some larger particle motions in more local events. Arrows mark the direction of motion, which is downhill, which also applies to the further images, i.e., to the left being downhill. Displacements end if the material is deposited. Therefore, the displacement maps also visualize the tracks of materials moving over some distance.

Figure 11 shows an event within the illuminated spot on the basalt sample. Figure 12 shows an example of motion tied to illumination on the JSC surface. These events are close to the shadow but not exceptionally close. It might be that for the current particle beds the mobility of particles and therefore specific location are more important than the proximity of a transition between light and shadow.

Another kind of event on a JSC sample is shown in Figure 13, where particle motion seems to be related to small cracks on the surface, also here within the illuminated spot. Overall, while we do not detect a clear, single static angle of repose, we detect inclination-related local motion events of various strengths.

5.2. Event Charts

Our basic motivation for the work reported here was to see the effects of illumination and variations thereof on particle motion on slopes under Martian conditions. In particular, we were interested in comparing the inclinations of slopes at the onset of particle motion with and without various variations in illumination and temperature going along with this. Therefore, we divided the events into those clearly outside the illumination

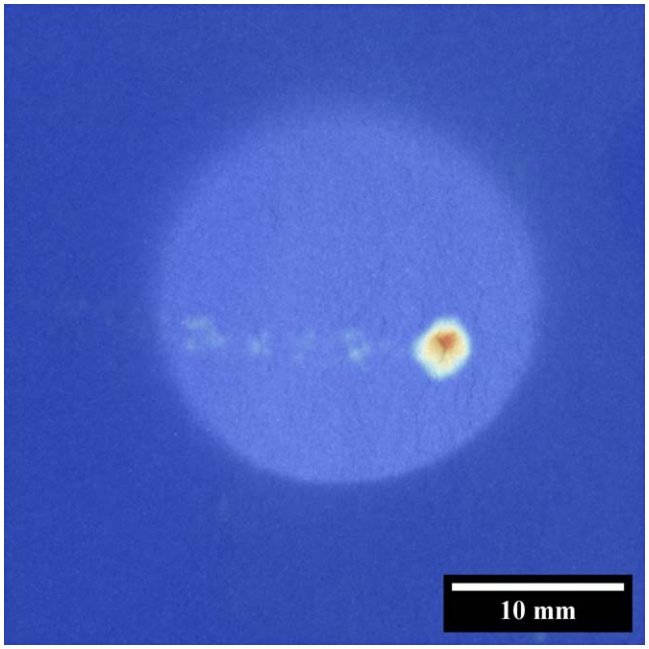

Figure 11. As Figure 10 but for one event inside the illuminated spot for basalt at 2 mbar (parabola Nr. 24, first day). The calculated displacement (color) is overlaid with the photo of the surface before the slide occurred. Yellow to red colors mark the positions of the grains that moved downwards (to the left). For better visibility the image is further contrast-enhanced.

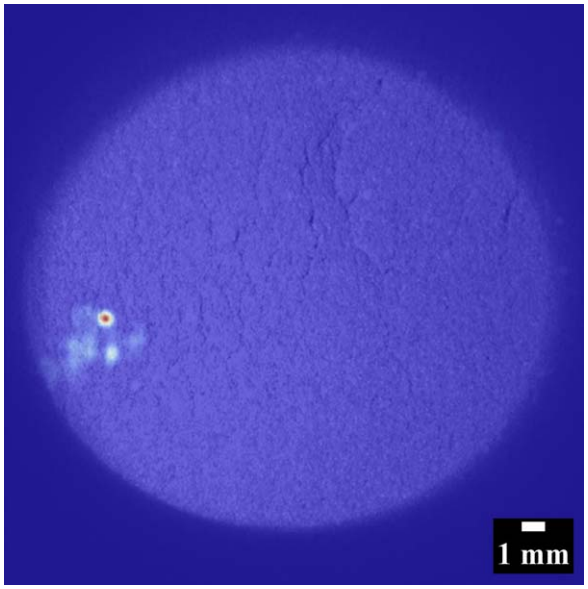

Figure 12. Weak slide inside the illuminated spot for JSC at 6 mbar (parabola Nr. 9, first day). The calculated displacement (color) is overlaid with the photo of the surface before the slide occurred. Yellow to red colors mark the positions of the grains that moved downwards (to the left). For better visibility the image is further contrast-enhanced.

or on nonilluminated particle beds and those within the illuminated spot.

On the first flight day, the angle was increased continuously from 0° to 45°. Pressure was essentially set in two ranges: 191 ± 9 Pa and 573 ± 24 Pa for JSC and 204 ± 11 Pa and 603 ± 26 Pa for basalt as the sample. These samples either were not illuminated or were continuously illuminated during low gravity in a spot with a light flux of 590 W m^{-2}, or in some cases around 1200 W m^{-2}.

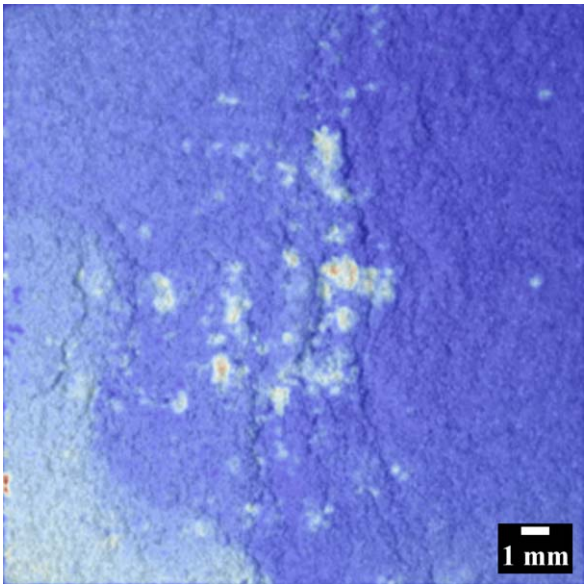

Figure 13. Particle movement around cracks inside the illuminated spot for JSC at 2 mbar (parabola Nr. 27, first day). The calculated displacement (color) is overlaid with the surface before the slide occurred. Yellow to red colors mark the positions of the grains that moved downwards (to the left). For better visibility the image is further contrast-enhanced.

Figures 14 and 15 show the observed particle motion events for varying inclination. One parabola can have several events as the slope angle is continuously increased at a rate of 2–3° s^{-1}. Events not obviously related to the illumination spot have square symbols, while those within the spot have circular symbols. Also added to the symbol is the number of the parabola (one flight has 31 parabolas) in which the event occurred.

5.2.1. JSC Mars 1a

Figure 14 shows the event chart for the JSC sample at 191 Pa ambient pressure. The data can be divided visually into three separated slope zones. There is an initial zone (1) at low inclinations. This can best be seen on the chart of basalt though (Figure 16), with frequent motion within this zone. This is shortly after the onset of the microgravity phase of the flight. As the initially downward facing gondolas still have to adjust to the gravity level (horizontal orientation), but can overshoot while swinging outwards, they sometimes hit a bumper that restricts their motion to the upper end. This induces vibrations, and we attribute any particle motion at these low angles to this motion, irrespective of illumination or not. We do have observations by eye but do not have any recordings that can restrict this transient phase further in time or strength, but it depends on the individual parabolas with their specific *g*-jitter profiles. Assuming this to be the initial ~2 s, it might correspond to about ~7° at most. Figure 14 then shows a further zone (2) up to about 20° where motion is only occurring within the illuminated spot. This is then followed by a third zone where motion is occurring irrespective of illumination.

Figure 15 shows the data for the same JSC sample but at 573 Pa. While all zones are filled by events attributed to illumination there is generally little "regular" motion not related to a light flux and it is only in zone (3). Therefore, the data are consistent with the three-zone picture observed at lower pressure.

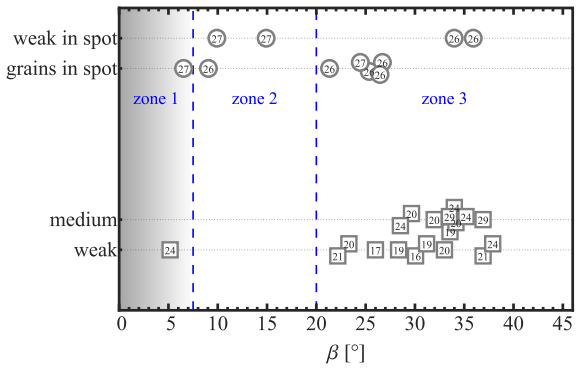

Figure 14. Event chart with particle motion for varying slope for JSC at 191 Pa ambient pressure and a light flux of 591 W m^{-2}. Strength of the event (left axis) is qualitatively related to the number of moving particles. Strength of the event: (1) grains: movement of single grains/aggregates, (2) weak: movement of a small area on a part of the surface, (3) medium: movement of a larger area on a part of the surface. Circles at the top mark events related to the light spot. Squares at the bottom mark events are not related to light. We divide the slope into three zones related to the transient beginning at low angles, the light-dominated zone, and the regular zone.

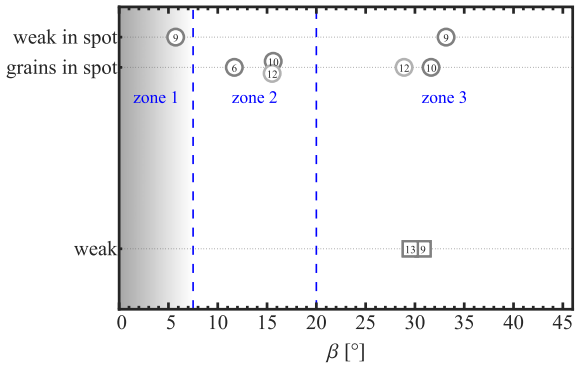

Figure 15. Same as Figure 14 (JSC) but at 573 Pa ambient pressure.

Overall, there is a clear tendency for this sample that events on the illuminated part of the surface occur at much lower inclinations. Events on illuminated slopes easily occur at angles 10° lower than in nonilluminated parts of the slope. This trend is even more pronounced when considering that the total nonilluminated area is much larger than the illuminated area, which adds some bias in favor for detecting events outside the spot.

5.2.2. Basalt

Figures 16 and 17 show the equivalent event charts for the basalt sample at 204 Pa and 603 Pa, respectively. Here, zone (1) is especially visible. However, particle motion not attributed to illumination reaches down to this zone for basalt, i.e., it is easy to move grains without the need for illumination and there is no clear zone (2).

In total there are only a few events specifically within the illuminated part, i.e., none at 204 Pa and only a few at 603 Pa. It has to be considered that not all parabolas had the light turned on and, again, it has to be considered that the nonilluminated area is larger. In view of the sparse data with respect to illumination and with zone (3) essentially reaching down to zone (1), the basalt sample does not provide information on the activity of a Knudsen compressor.

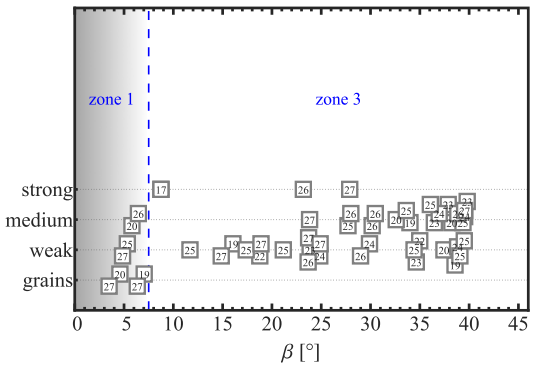

Figure 16. Same as Figure 14 but for basalt and 204 Pa. No events could be detected within the illuminated spot here.

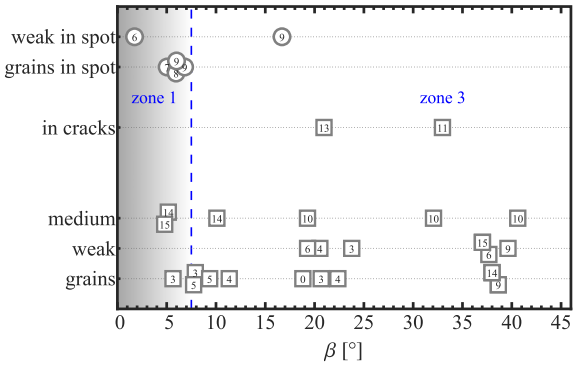

Figure 17. Same as Figure 16 for basalt but at 603 Pa. Some motion is seen within the light spot but there is no correlation to small slopes in comparison to the motion outside the spot.

5.3. Lights Off

On the second and third flight days, we started with higher inclination angles (⩾20°) for various technical reasons. The data produced therefore do not provide new insights into zone (2), which is the relevant one here. However, we tested the effect that particles move if the light is turned off. Indeed, in these cases we could frequently observe strong events of particle motion shortly after turning off the light. Figure 19 (top) shows one of these events as an overlay of the image of the spot to indicate the place where the spot was, and the sum of displacements calculated for the successive frames in the video and the initial frame.

As particle motion might be related to slope angle, temperature, and time, we determined the respective values for when the light was turned off and when motion is observed. The observations we made are summarized in Figure 18. The initial angle set in level flight and the transition of this inclined surface to low gravity did not induce particle motion. In fact, there are also parabolas with no motion at all. We also added these nonevents, i.e., parabolas, where no motion was observed after the light was turned off during Martian gravity. Each continuous or dashed arrow represents an event or nonevent, respectively. Each arrow corresponds to one parabola. For the given parabola the arrow starts at T_{max} (mean temperature inside the spot right before the light is switched off) and the mean initial angle. The arrow ends at the temperature when the event starts (for an event) or at the temperature at the end of Martian gravity (for a nonevent) and the corresponding angle. The motion events do not start right at the moment the illumination is switched off but after a delay of a few seconds.

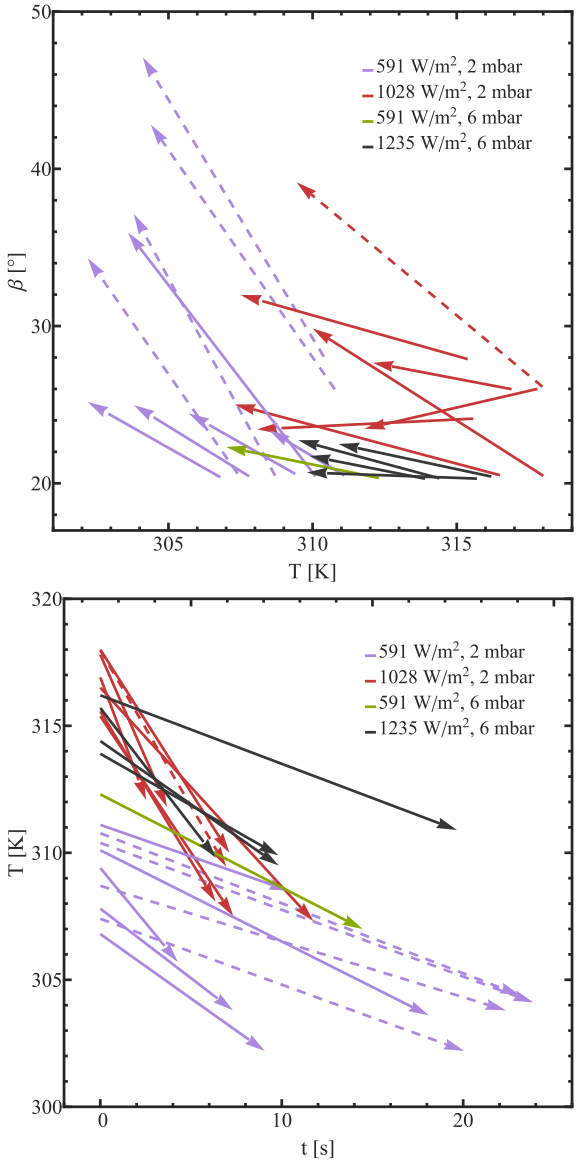

Figure 18. Top: each arrow represents an event (continuous line) or nonevent (dashed line) occurring for JSC at 204 Pa and 603 Pa and the light intensities of 591 W m^{-2}, 1028 W m^{-2}, and 1235 W m^{-2}. Each arrow corresponds to one parabola. For the given parabola the arrow starts at T_{max} (mean temperature inside the spot when the light is switched off) and the mean initial angle. The arrow ends at the temperature when the event starts (for an event) or at the temperature at the end of Martian gravity (for a nonevent) and the corresponding angle. Note the limited amount of data for 603 Pa. Bottom: time elapsed after the light was switched off and until the event occurs/the Martian gravity ends for the events/nonevents from the top panel.

The delays for the occurrences shown in the top panel of Figure 18 can be extracted from the bottom panel of that figure. To be able to compare the nonevent to the event we take the time between when the light was switched off and the end of Martian gravity (t_{end}) or the final slope angle. We do so because the limited time we have Martian gravity on the plane can be the main constraint for the event to not occur. If the time were not limited, the event could still occur; the compaction of the dust bed is slightly different for each parabola, so more time might be needed to initiate the event.

For better visibility there are no error bars in Figure 18. The error for β was always below 7% of the β-value, whereas the temperature error was smaller than 2.2% of the measured value. According to the manufacturer, the thermal camera used has an accuracy of ± 5 K from the reading, which is a systematic error. This only has an influence on the absolute value and not on the temperature difference, as the thermal resolution of the IR camera is 0.01 K.

We know this kind of particle motion after a light source is shut off from ground-based ($1g$) lab experiments but we could never observe this at such a low light flux. So far, we have studied this on flat surfaces and always required rather about 5 kW m^{-2}. Now at reduced gravity and with increasing slopes, illumination and variation thereof clearly lead to the ejection and downhill motion of particles at the Martian illumination level at least down to 591 W m^{-2}. While we do not have a one-to-one comparison with the sample used on the flight reported here, this is about a factor of 10 less than in those earlier experiments.

Illumination of the dust bed changes its temperature. An example of the surface temperature taken with an IR camera is shown in Figure 19 (middle). The thermal image was taken right before the illumination was turned off. One can notice a somewhat uneven temperature distribution inside the spot, which is due to the fact that the illuminating optic was placed slightly inclined toward the surface normal of the dust bed. Figure 20 shows the temperature profile along the center of the spot in the horizontal direction. The temperature maximum is shifted to the left half of the spot, to the site where all of the movements originate from (compare the top and bottom panels of Figure 19).

Figure 21 shows the typical change in the mean temperature inside the spot during one parabola. The light blue area marks the time during the nearly constant Martian gravity. All the events take place during this phase.

5.4. Discussion

We did not see slides at the size scale of the particle bed except in rare cases of very steep angles (45°) and strong accelerations, e.g., in the case of the return from Martian gravity to hypergravity at the end of parabolas. However, the current samples we chose (grain size, material) were not preselected with respect to low angles of repose. In fact, we knew from preliminary tests that they would only start to collapse at very high angles, if at all. Also, the beds were horizontally vibrated often during the flight (after every parabola) to prepare a flat surface. This likely compacted most of the bed. Therefore, the current data do not allow classification of classical angle of repose for the particle bed.

This still leaves parts of the top layers as sources of less bound particles to which the force balance above can be applied to test our hypothesis that the illumination profile should influence the angle at which particles start moving. In this respect, we compare the local events here. As such, they are likely not representative of an angle of repose in general, which explains rather low slopes for particle motion. Nevertheless, our data show the slope where events are triggered with or without light.

For the JSC particle bed, we see a reduction of the slope where particle motion is observed by about 10° within an illuminated part of the particle bed. As nonilluminated JSC has a rather sharp limit of motion beyond 20°, this can be considered a firm finding. With earlier laboratory experiments showing that light can induce particle lift (de Beule et al. 2014), this is something to expect, but for the first time, due to the

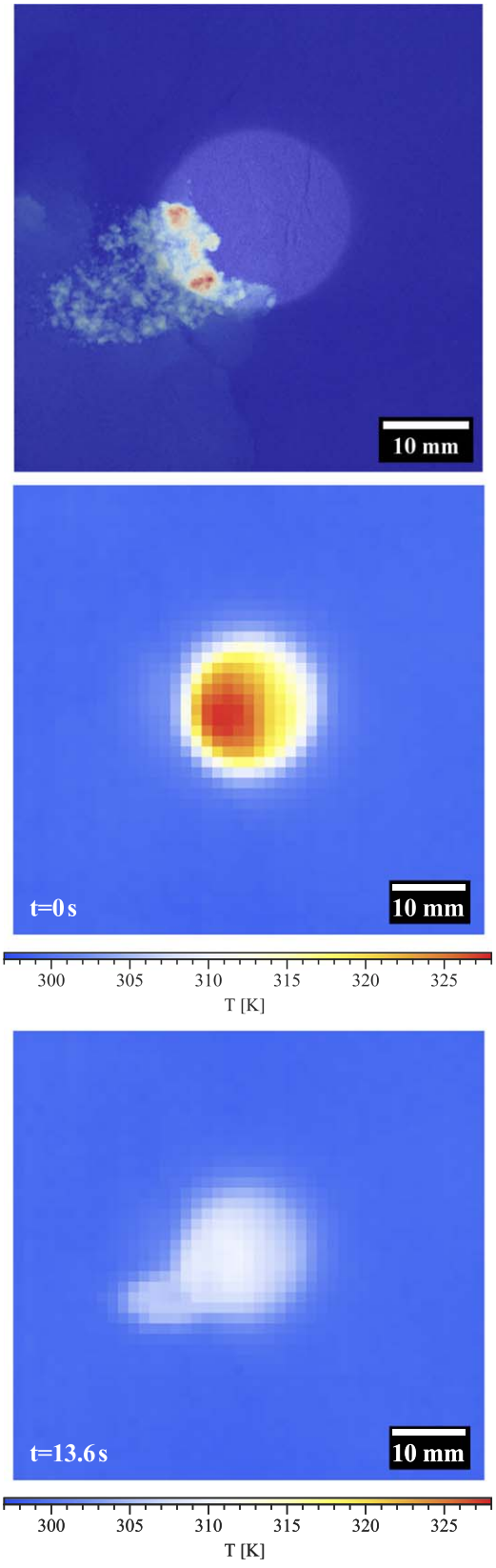

Figure 19. Top: color-coded visualization of particle motion after the light was switched off for JSC at 2 mbar (parabola Nr. 16, second day). The blue color symbolizes the area with very weak to no displacement. Middle: thermal camera image of the area around the spot at the moment right before the light was switched off. Bottom: thermal camera image for one of the later times, showing particle movement.

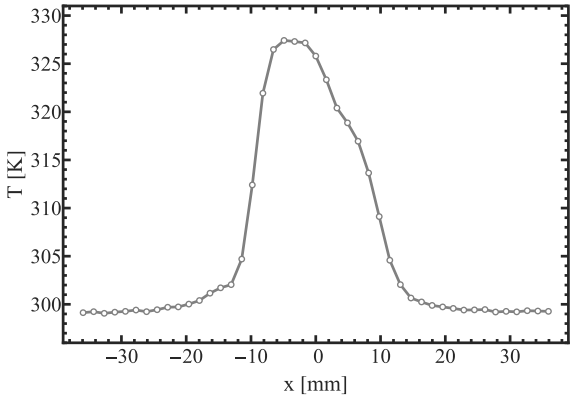

Figure 20. Temperature profile along the middle of the spot right before the light (intensity of 1043 W m^{-2}) is switched off. JSC at 2 mbar (parabola Nr. 16, second day). The middle of the spot is set to $x = 0$ mm.

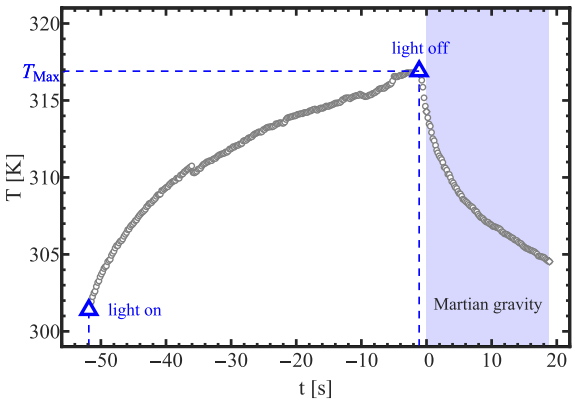

Figure 21. Average temperature inside the spot over time. T_{max} indicates the time when the light is switched off. The light blue area marks the part of nearly constant Martian gravity. The negative time corresponds to the time before the constant Martian gravity occurs. JSC at 2 mbar (parabola Nr. 16, second day) illuminated by the light of 1043 W m^{-2} intensity.

inclined slope and Mars gravity, we really see this effect being triggered at an intensity reaching down to the Martian insolation flux.

We do not see particle motion clearly associated with the sharp transition of the light spot to the surrounding shadows as expected (Schmidt et al. 2017). The data are still sparse, however, and motion is observed "close" to the shadow. So, the experiments neither rule out nor confirm a spatial setting yet.

In some cases, the motion seems to be related to small cracks. So while this is not directly the case proposed by Schmidt et al. (2017), it might be a mechanism similar to that of having a nearby gas reservoir to draw upon.

Basalt did not show a specific slope for general particle motion without light, but particles moved without illumination at essentially all angles. Therefore, this sample was not suited for our case. The MGS sample essentially did not move at all, excluding a few larger loose sand grains sliding down the surface, likely due to compaction, and therefore gave neither positive nor negative verification of the effect. We must stress here that this is the only sample that was not heated before use and it has on average larger particles, as it was not sieved.

We again note that the vibrations that flattened the particle beds seemed to compact the granular medium to a point where most of the bed got stuck within the container, except for the top layers.

Therefore, none of the particle beds showed the expected static angle of repose around 30°–40° at which failure should lead to large-scale avalanches. This only occurred if the bed experienced a strong mechanical pulse during deceleration by hitting the structure. This launched large-scale downflow. The samples are also sensitive to humidity and show worse flowability when stored in a humid environment. The basalt and the JSC-1 sample were heated prior to the experiments to reduce this effect. What we observe is motion within the top layers of the particle bed, which are not compacted. Due to their thin nature, independent local particle motion can occur. If the particles on top are more mobile, they might move downwards at already low angles. This is the case for basalt. In the case of basalt, we could observe some clumps (aggregates) on top of a "smooth" surface, which also indicates the cohesive nature of this sample. Some of the clumps can also slide down at lower angles. If the top layer is part of the compacted bed, no particle motion can be detected. This is the case for MGS. Only if the top layer has a mobility similar to the expected static angles of repose do the measurements allow us to quantify a difference depending on illumination or not. This is the case for the JSC sample. For JSC we did quantify the compaction because the initial sample had an initial filling factor of $0.87 \pm 0.02\,\mathrm{g\,cm^{-3}}$ while the vibrations lead to $1.07 \pm 0.02\,\mathrm{g\,cm^{-3}}$. Vibrations might induce a "Brazil nut" effect, with large particles moving to the top. This would not be visible in our camera images and we have not evaluated these effects yet.

Another interesting finding was the reaction of the particle bed to the switching off of the illumination. As also seen in earlier laboratory experiments, this can induce rather strong Knudsen compressors (Kelling et al. 2011; Kocifaj et al. 2011; Kuepper & Wurm 2016). Also here, we saw clear motion of grains within a preilluminated spot shortly after the light was turned off. Again, where we needed several $\mathrm{kW\,m^{-2}}$ on a flat sample under 1*g* before, we now see ejection of grains at Martian light flux. It is currently not clear how this relates to a Martian application as usually sunlight is not shut off very rapidly. Most plausibly, a cloud from a dust devil might suffice to trigger this effect. Also, self-shadowing might amplify an avalanche. These are currently speculations, however.

Basalt and MGS samples did not provide further information on thermal creep effects. In any case, we consider the observation of an easier JSC particle motion within the light and the ejection once the light source is shut off as support for active Knudsen pumps on Mars.

5.4.1. Unknowns

There are some factors that might be important that we could not test. For one thing, the duration of illumination is only some tens of seconds. On Mars, the Sun might have much longer to set temperature gradients, and this might strengthen a Knudsen compressor. We also did not work at low temperatures. Colder conditions, however, might be good for the effect. Laboratory experiments showed that, for example, levitation of grains also works for water ice (Aumatell & Wurm 2011). Humidity was not controlled in the experiments or samples. This can be important for sticking forces and absolute values (Pillich et al. 2021). With the moderate light fluxes and surface temperatures considered, we do not expect that water itself, e.g., as vapor, would play a part in the measurements. Last, we did use air and not CO_2 but we consider this to be a concern only for the specific pressure dependence of the effect.

6. Conclusions

We carried out a first set of experiments on parabolic flights to study conditions under which particles move downhill on Martian slopes. We simulated Martian gravity, Martian surface pressure, and Martian insolation. Altogether, being as close to Martian conditions as possible, we could show that these conditions are sufficient to induce Knudsen compressors within the Martian soil simulant.

As discussed in the introduction, our motivation originates partially from the debate on whether the measured static angles of repose for RSLs or other slopes are the same on Mars and Earth and whether Knudsen compressors can decrease them if the setting is right. Our first sample beds here do not allow a general statement, as the compaction of the particle beds did not allow us to measure a clear angle of repose. We did find significant particle motion related to illumination though. For the JSC Mars 1a sample, we found motion within the light spot at slopes about 10° less than in a dark part of the surface. This is clearly supportive of a Knudsen compressor to apply a lifting force on particles within the top layers. We also found a clear amplification of particle lift, i.e., strong ejection of grains, if the light source was turned off after it had heated the slope for a while. Both kinds of effects—particle lift under continuous illumination and amplification of particle lift if the light source was turned off—were known from ground-based experiments. At 1*g* on a flat particle bed, motion is only triggered at a light flux of several $\mathrm{kW\,m^{-2}}$ though. Therefore, it is certainly one of the most important findings of these first experiments under Martian conditions that particle motion is already triggered at a light flux about a factor of 10 lower, i.e., at a few hundred $\mathrm{W\,m^{-2}}$ as present on Mars.

Thermal creep and Knudsen compressors related to sunlight doubtless are an efficient particle lifting mechanism on Martian slopes. Even if we could not pin them down as reducing angles of repose for RSLs or other slopes on Mars, with the current experimental setup at least, these effects provide sources of atmospheric dust in any case, apart from large-scale slides. Particle motion can be initiated on slopes much shallower than the static angle of repose.

Acknowledgments

This project is supported by DLR Space Administration with funds provided by the Federal Ministry for Economic Affairs and Climate Action (BMWK) under grant Nos. 50WM2049 and 50WK2270C. This project also has received funding from the European Union's Horizon 2020 research and innovation program under grant agreement No 101004052. We thank Jani Radebaugh and an anonymous referee for a constructive review of our manuscript.

ORCID iDs

Tetyana Bila https://orcid.org/0000-0001-6653-7255
Gerhard Wurm https://orcid.org/0000-0002-7962-4961
Kolja Joeris https://orcid.org/0000-0002-5841-2636
Jens Teiser https://orcid.org/0000-0003-4468-4937

References

Aharonson, O., Schorghofer, N., & Gerstell, M. F. 2003, JGRE, 108, 5138
Attree, N., Kaufmann, E., & Hagermann, A. 2021, Icar, 359, 114355
Atwood-Stone, C., & McEwen, A. S. 2013, GeoRL, 40, 2929
Aumatell, G., & Wurm, G. 2011, MNRAS, 418, L1

Becker, T., Teiser, J., Jardiel, T., et al. 2022, PSJ, 3, 195
Bila, T., Kollmer, J., Teiser, J., & Wurm, G. 2023, PSJ, 4, 16
Bridges, N., Ayoub, F., Avouac, J.-P., et al. 2012a, Natur, 485, 339
Bridges, N. T., Bourke, M. C., Geissler, P. E., et al. 2012b, Geo, 40, 31
Cannon, K. M., Britt, D. T., Smith, T. M., Fritsche, R. F., & Batcheldor, D. 2019, Icar, 317, 470
Cantor, B., James, P., Caplinger, M., & Wolff, M. 1999, JGR, 106, 23653
Chojnacki, M., Burr, D., Moersch, J., & Michaels, T. 2011, JGRE, 116, E00F19
Chojnacki, M., McEwen, A., Dundas, C., et al. 2016, JGRE, 121, 1204
de Beule, C., Wurm, G., Kelling, T., et al. 2014, NatPh, 10, 17
de Beule, C., Wurm, G., Kelling, T., Koester, M., & Kocifaj, M. 2015, Icar, 260, 23
Deshpande, N. S., Furbish, D. J., Arratia, P. E., & Jerolmack, D. J. 2021, NatCo, 12, 3909
Divoux, T., Gayvallet, H., & Géminard, J.-C. 2008, PhRvL, 101, 148303
Dundas, C. M. 2020, Icar, 343, 113681
Dundas, C. M. 2021, in Mars Geological Enigmas: From the Late Noachian Epoch to the Present Day, ed. R. J. Soare et al. (Amsterdam: Elsevier), 263
Elekes, F., & Parteli, E. J. R. 2021, PNAS, 118, e2107965118
Ewing, R. C., Lapotre, M. G. A., Lewis, K. W., et al. 2017, JGRE, 122, 2544
Greeley, R., Leach, R., White, B., Iversen, J., & Pollack, J. 1980, GeoRL, 7, 121
Heyer, T., Raack, J., Hiesinger, H., & Jaumann, R. 2020, Icar, 351, 113951
Johnson, K. L., Kendall, K., Roberts, A. D., & Tabor, D. 1971, RSPSA, 324, 301
Kaufmann, E., Kömle, N. I., & Kargl, G. 2006, Icar, 185, 274
Kelling, T., Wurm, G., Kocifaj, M., Klačka, J., & Reiss, D. 2011, Icar, 212, 935
Kleinhans, M. G., Markies, H., de Vet, S. J., in't Veld, A. C., & Postema, F. N. 2011, JGRE, 116, E11004
Knudsen, M. 1909, AnP, 336, 205
Kocifaj, M., Klačka, J., Kelling, T., & Wurm, G. 2011, Icar, 211, 832
Koester, M., Kelling, T., Teiser, J., & Wurm, G. 2017, Ap&SS, 362, 171
Kok, J. F., Parteli, E. J. R., Michaels, T. I., & Karam, D. B. 2012, RPPh, 75, 106901
Kok, J. F., & Renno, N. O. 2008, PhRvL, 100, 014501
Kuepper, M., & Wurm, G. 2016, Icar, 274, 249
Lange, L., Forget, F., Dupont, E., et al. 2023, JGRE, 128, e2023JE007915
Lorenz, R. D. 2023, JGRE, 128, e2023JE007843
McEwen, A. S., Ojha, L., Dundas, C. M., et al. 2011, Sci, 333, 740
McEwen, A. S., Schaefer, E. I., Dundas, C. M., et al. 2021, JGRE, 126, e06575
Montabone, L., Lewis, S., & Read, P. 2005, AdSpR, 36, 2146
Muntz, E. P., Sone, Y., Aoki, K., Vargo, S., & Young, M. 2002, JVSTA, 20, 214
Musiolik, G., de Beule, C., & Wurm, G. 2017, Icar, 296, 110
Philippe, M., Conway, S. J., Raack, J., et al. 2023, Icar, 395, 115475
Pillich, C., Bogdan, T., Landers, J., Wurm, G., & Wende, H. 2021, A&A, 652, A106
Reiss, D., & Lorenz, R. 2016, Icar, 266, 315
Reiss, D., Raack, J., Rossi, A. P., Di Achille, G., & Hiesinger, H. 2010, GeoRL, 37, L14203
Schmidt, F., Andrieu, F., Costard, F., Kocifaj, M., & Meresescu, A. G. 2017, NatGe, 10, 270
Schorghofer, N., & King, C. M. 2011, Icar, 216, 159
Stillman, D. E., Bue, B. D., Wagstaff, K. L., et al. 2020, Icar, 335, 113420
Stillman, D. E., Michaels, T. I., Hoover, R. H., et al. 2021, Icar, 369, 114648
Tebolt, M., Levy, J., Goudge, T., & Schorghofer, N. 2020, Icar, 338, 113536
Toledo, D., Apéstigue, V., Arruego, I., et al. 2023, JGRE, 128, e2022JE007494
Vargo, S. E., Muntz, E. P., Shiflett, G. R., & Tang, W. C. 1999, JVSTA, 17, 2308
Vicente-Retortillo, A., Martínez, G. M., Lemmon, M. T., et al. 2023, JGRE, 128, e2022JE007672
Wurm, G., & Krauss, O. 2006, PhRvL, 96, 134301

DOI: 10.3847/PSJ/ad3df4
URN: urn:nbn:de:hbz:465-20250110-111442-3